


Midinfrared Emission and Absorption in Strained and Relaxed Direct-Band-Gap $\text{Ge}_{1-x}\text{Sn}_x$ Semiconductors

S. Assali^{1,*}, A. Dijkstra^{2,†}, A. Attiaoui¹, É. Bouthillier¹, J.E.M. Haverkort², and O. Moutanabbir¹

¹*Department of Engineering Physics, École Polytechnique de Montréal, C. P. 6079, Succ. Centre-Ville, Montréal, Québec H3C 3A7, Canada*

²*Department of Applied Physics, Eindhoven University of Technology, 5600 MB Eindhoven, Netherlands*

 (Received 26 April 2020; revised 21 December 2020; accepted 22 December 2020; published 12 February 2021)

By independently engineering strain and composition, this work demonstrates and investigates direct-band-gap emission in the midinfrared range from $\text{Ge}_{1-x}\text{Sn}_x$ layers grown on silicon. We extend the room-temperature emission wavelength above approximately $4.0 \mu\text{m}$ upon postgrowth strain relaxation in layers with uniform Sn content of 17 at.%. The fundamental mechanisms governing the optical emission are discussed based on temperature-dependent photoluminescence, absorption measurements, and theoretical simulations. Regardless of strain and composition, these analyses confirm that single-peak emission is always observed in the probed temperature range of 4–300 K, ruling out defect- and impurity-related emission. Moreover, carrier losses into thermally activated nonradiative recombination channels are found to be greatly minimized as a result of strain relaxation. Absorption measurements validate the direct band-gap in strained and relaxed samples at energies closely matching photoluminescence data. These results highlight the strong potential of $\text{Ge}_{1-x}\text{Sn}_x$ semiconductors as versatile building blocks for scalable, compact, and silicon-compatible midinfrared photonics and quantum optoelectronics.

DOI: [10.1103/PhysRevApplied.15.024031](https://doi.org/10.1103/PhysRevApplied.15.024031)

I. INTRODUCTION

Free-space communications, infrared harvesting, biological and chemical sensing, and imaging technologies would strongly benefit from the availability of scalable, cost-effective, and silicon- (Si-) compatible midinfrared (MIR) optoelectronic devices. With this perspective, Sn-containing group-IV semiconductors $\text{Si}_y\text{Ge}_{1-x-y}\text{Sn}_x$ grown on Si wafers have recently been the subject of extensive investigations [1–5]. At the core of these expended efforts is the ability to harness the efficient direct-band-gap emission from these emerging semiconductors, which can be achieved at a Sn content around 10 at. % in fully relaxed layers. It is, however, noteworthy that this critical composition is significantly above the approximately 1 at. % equilibrium solubility of Sn in Ge, which calls for a precise control of the growth kinetics to prevent phase separation and avoid Sn segregation and material degradation. Moreover, the epitaxial growth of $\text{Ge}_{1-x}\text{Sn}_x$ is typically achieved on Si wafers using a Ge interlayer, commonly known as Ge virtual substrate (Ge-VS), resulting in inherently compressively strained $\text{Ge}_{1-x}\text{Sn}_x$ [6,7]. This residual compressive strain increases the Sn content threshold for

the indirect-to-direct band-gap crossover and the associated optical emission is shifted to higher energies relative to that of a relaxed material [8–10]. Moreover, the accumulated strain in $\text{Ge}_{1-x}\text{Sn}_x$ epitaxial layers was found to affect the incorporation of Sn throughout the growth, which can lead to graded composition as layers grow thicker [6,7].

Among the strategies to circumvent $\text{Ge}_{1-x}\text{Sn}_x$ growth hurdles, lattice-parameter engineering using multilayer and step-graded growth has been shown to be effective in controlling the Sn content and its uniformity. This process was exploited in recent studies demonstrating room-temperature optical emission down to 0.36 eV (approximately $3.4 \mu\text{m}$ wavelength) [4], as well as optically and electrically pumped lasers at short-wave IR (SWIR)-MIR wavelengths operating at lower temperatures [11–13]. Postgrowth control and manipulation of strain have also been utilized to extend the emission range as longer emission wavelengths can be achieved through relaxation and tensile-strain engineering [2–4,11,14–17].

Notwithstanding contributions from the aforementioned studies, in-depth investigations of $\text{Ge}_{1-x}\text{Sn}_x$ optical emission are, however, still in their infancy. Besides the ability to engineer innovative optoelectronic devices, the availability of high-quality $\text{Ge}_{1-x}\text{Sn}_x$ layers also provides a rich playground to explore and uncover their fundamental properties and probe their behavior as a function of key parameters, namely temperature, strain, and composition.

*simone.assali@polymtl.ca

†These authors contributed equally to this work.

As mentioned above, strain and composition are always interrelated in epitaxial $\text{Ge}_{1-x}\text{Sn}_x$ layers. Here, we decouple and elucidate their individual effects on the optical emission of $\text{Ge}_{1-x}\text{Sn}_x$ by performing systematic studies on the optical emission of strained and relaxed $\text{Ge}_{1-x}\text{Sn}_x$ in the 4–300 K range. The emission spectra are then discussed in the light of $8 \times 8 \mathbf{k} \cdot \mathbf{p}$ band-structure calculations and absorption measurements. We find that the optical emission wavelength at room temperature can be extended above $4 \mu\text{m}$ upon significant postgrowth relaxation of the compressive strain in underetched $\text{Ge}_{0.83}\text{Sn}_{0.17}$. By cooling down to 4 K, the single emission peak is preserved in both strained and relaxed layers, indicative of the direct band-gap emission across the entire temperature range. Thermally activated nonradiative recombination channels are found to have a negligible effect on the emission of $\text{Ge}_{0.83}\text{Sn}_{0.17}$ and no additional impurity-related emission is observed upon relaxation. Interestingly, in relaxed $\text{Ge}_{0.83}\text{Sn}_{0.17}$, the reduction in PL intensity at 300 K is relatively limited and the measured intensity is approximately 10% of that recorded at 4 K. Similar behavior is found in lower Sn content layers $\text{Ge}_{0.863}\text{Sn}_{0.137}$, with an initial in-plane compressive strain of -0.4% . By performing absorption measurements, the contribution of layers with different composition can be precisely decoupled. These measurements confirm the recorded behavior of PL emission energy upon lattice relaxation, thus providing an additional demonstration of the band-gap directness in both strained and relaxed $\text{Ge}_{0.83}\text{Sn}_{0.17}$ samples, as well as in the relaxed $\text{Ge}_{0.863}\text{Sn}_{0.137}$.

II. METHODS

The layers investigated in this work are grown on 4-in. Si (100) wafers in a low-pressure chemical vapor deposition (CVD) reactor using ultrapure H_2 carrier gas, and 10% monogermane (GeH_4) and tin-tetrachloride (SnCl_4) precursors, following a recently developed growth protocol [4,7,18,19]. First, a 600–700 nm-thick Ge-VS is grown at 450°C , followed by thermal cyclic annealing ($>800^\circ\text{C}$) and additional Ge deposition. The $\text{Ge}_{0.83}\text{Sn}_{0.17}$ sample with a uniform composition is grown using a $\text{Ge}_{1-x}\text{Sn}_x$ multilayer heterostructure, where the incorporation of Sn is controlled by the growth temperature [18]. The 17 at. % top layer (TL), 12–10 at. % middle layer (ML), and 8 at. % bottom layer (BL) are grown at 280, 300, and 320°C , respectively, with a TL/ML/BL thicknesses of 160/155/65 nm [4]. In the compositionally graded $\text{Ge}_{0.863}\text{Sn}_{0.137}$ sample, a 8 at. % buffer layer (320°C) with a thickness of approximately 60 nm is used for the subsequent growth of the (graded uniform) 10.5/12.9–13.7 at. % layer at 300°C on top [19]. To relax the epitaxial strain, the grown layers are released from the substrates by patterning and underetching microdisks. First, $7\text{-}\mu\text{m}$ -wide disks are defined in ma-N 2410 resist with electron-beam lithography. Microdisks are

patterned with a $10 \mu\text{m}$ pitch over $2.5 \times 2.5 \text{ mm}^2$ arrays. This is followed by two successive reactive ion-etching (RIE) steps. First, a Cl_2 -based plasma is used to vertically etch the $\text{Ge}_{1-x}\text{Sn}_x$ layer and transfer the resist pattern to the Ge-VS. Second, Ge is selectively etched in a CF_4 -based plasma, resulting in released $\text{Ge}_{1-x}\text{Sn}_x$ microdisks.

The luminescence properties of the samples are measured using a FTIR-based photoluminescence setup [4]. The investigated samples are mounted in a vertically oriented helium flow cryostat with accurate temperature control. The samples are then illuminated using a 35-kHz-modulated cw 976-nm laser to allow for lock-in technique. The laser is focused using a 20.3-mm focal length, off-axis parabolic mirror, which also collected the PL signal and coupled it through the FTIR system, which is equipped with a $\text{Hg}_{1-x}\text{Cd}_x\text{Te}$ detector and a potassium bromide beam splitter. The full path of the PL emission is nitrogen purged to prevent water absorption lines in the measured spectra. To filter out the laser from the PL signal a germanium window is used as a long-pass filter. The PL measurements on the as-grown samples are performed at an excitation density of approximately 1 kW/cm^2 , while a higher value of 4 kW/cm^2 is used for the microdisks. To derive the Arrhenius parameters in a comparable way, all samples are measured at 4 kW/cm^2 . The absorption spectra are measured by coupling a light source through a Thermo Scientific Nicolet IS50R FTIR system, focusing it through a sample into a gold-coated integrating sphere and collected at a baffled port using a liquid-nitrogen-cooled Hg-Cd-Te detector. As a light source a LEUKOS ELECTRO MIR 4.1 supercontinuum laser is used for the as-grown $\text{Ge}_{0.83}\text{Sn}_{0.17}$ and $\text{Ge}_{0.863}\text{Sn}_{0.137}$ samples and a glowbar for the microdisk etched $\text{Ge}_{0.83}\text{Sn}_{0.17}$ sample because the absorption edge shifted out of the spectrum of the supercontinuum. The full optical path could not be purged with N_2 therefore background spectra are measured directly before every transmission measurement. A schematic of the used setup for this experiment is shown in Fig. S1 within the Supplemental Material [20].

III. RESULTS AND DISCUSSION

A. Fabrication and band structure of highly relaxed $\text{Ge}_{0.83}\text{Sn}_{0.17}$

Figure 1(a) exhibits a cross-section STEM image of the $\text{Ge}_{1-x}\text{Sn}_x$ 17/12/8 at. % (TL/ML/BL) multilayer stacking, with thicknesses of 160/155/65 nm [4], grown on Ge-VS/Si substrate. The composition of each layer is estimated from reciprocal space mapping (RSM) around the asymmetrical (224) XRD peak [Fig. 1(b)]. We note that the Sn content values obtained from the RSM map can be underestimated by 0.5–1.0 at. % as compared to values obtained using atom-probe tomography measurements [4]. This difference may come from the difference in

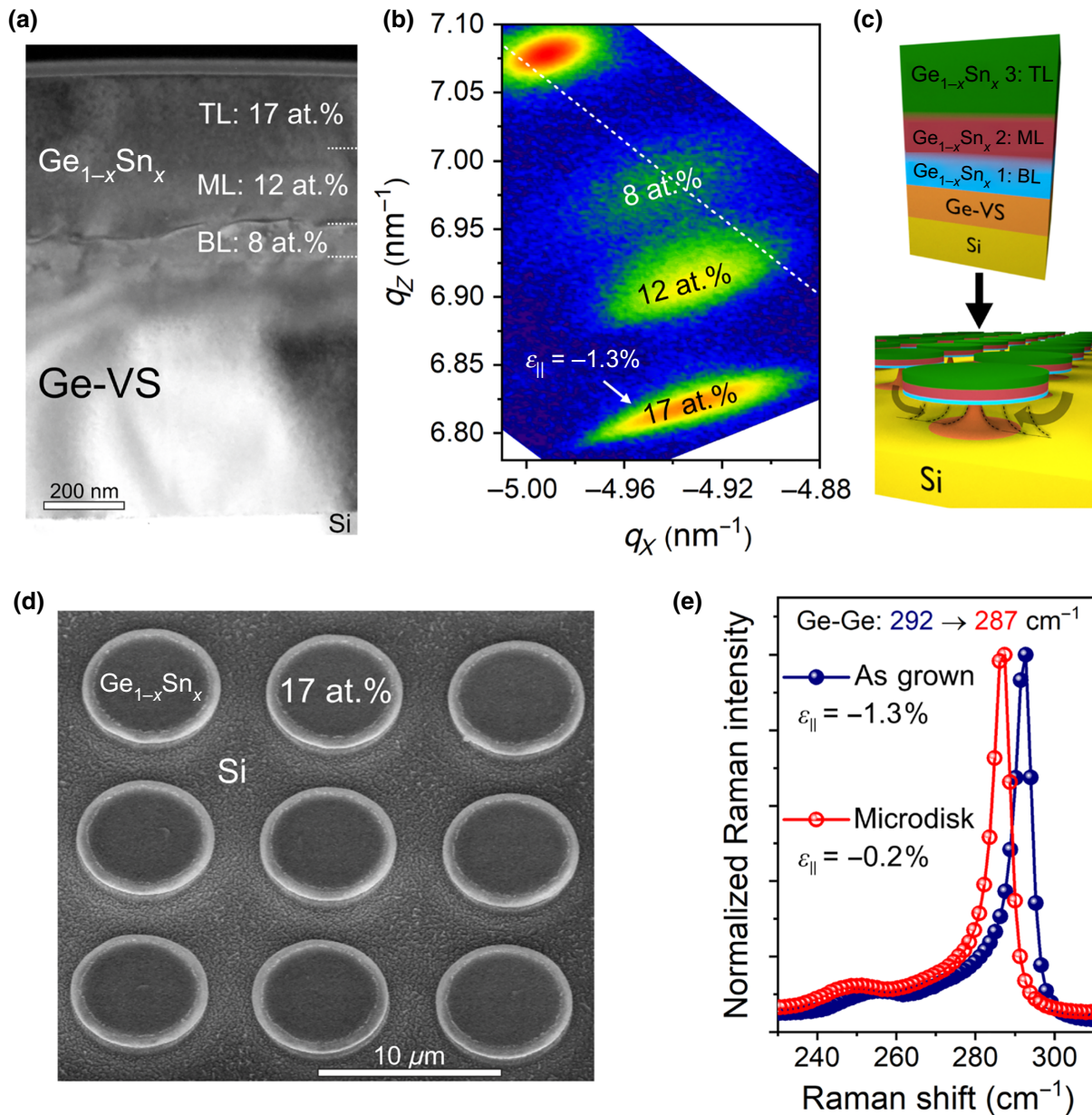


FIG. 1. (a) Cross-sectional TEM image along the [110] zone axis of the $\text{Ge}_{1-x}\text{Sn}_x$ 17/12/8 at. % (TL/ML/BL) multilayer stacking grown on the Ge-VS/Si substrate. Adapted from Ref. [4]. (b) XRD RSM around the asymmetrical (224) reflection for the as-grown $\text{Ge}_{0.83}\text{Sn}_{0.17}$ sample. Adapted from Ref. [4]. (c) Schematics of the microdisk fabrication process. (d) SEM image of the $\text{Ge}_{0.83}\text{Sn}_{0.17}$ microdisks (45° tilting angle). (e) Normalized Raman spectra for $\text{Ge}_{0.83}\text{Sn}_{0.17}$ acquired on the as grown (blue curve) and on the central portion of the microdisk (red curve).

the volumes analyzed by each technique. For consistency, compositions extracted from RSM are employed as they are averaged over a volume comparable to that probed in PL studies. The RSM data indicate that the TL is under an in-plane biaxial compressive strain $\varepsilon_{||} = -1.3\%$. As mentioned in the previous section, to significantly relax this residual strain, it suffices to release the $\text{Ge}_{1-x}\text{Sn}_x$ layers by etching away the underlying Ge-VS, as illustrated in Fig. 1(c). The SEM image in Fig. 1(d) shows a typical

array of microdisks having a diameter of $7\ \mu\text{m}$ and a pitch of $10\ \mu\text{m}$. The CF_4 etching time is selected to completely release the $\text{Ge}_{1-x}\text{Sn}_x$ microdisks, which collapse onto the Si wafer. We note that a small residual thickness of the Ge-VS layer is visible on the Si substrate underneath the microdisk after the fabrication process (Fig. S2 within the Supplemental Material [20]), which does not affect the strain in the microdisks because they are detached from the substrate.

Raman measurements are performed on the microdisk arrays to evaluate the residual strain in the $\text{Ge}_{1-x}\text{Sn}_x$ TL. Note that Raman spectra are recorded from the TL without any contribution from the underlying layers as the penetration depth of the 633-nm excitation laser (<30 nm) is significantly smaller than the TL thickness (160 nm) [4]. Figure 1(e) displays Raman spectra acquired at the center of a single microdisk (red curve). As a reference, the Raman spectrum of the as-grown $\text{Ge}_{0.83}\text{Sn}_{0.17}$ layer is also shown (blue curve). The Ge-Ge LO mode of the as-grown layer is centered at approximately 292 cm^{-1} , whereas the same mode shifts down to approximately 287 cm^{-1} in the underetched microdisks. The observed approximately 5 cm^{-1} shift corresponds to a strain relaxation from the as-grown value of -1.3% down to -0.2% in the microdisks. Note that Raman spectra associated to the area between microdisks show only the Si-Si LO mode at 520 cm^{-1} from the substrate (Fig. S2 within the Supplemental Material [20]), indicating that the Ge-VS is completely etched leading to the observed strain relaxation. The measured residual strain (-0.2%) in the TL even after the complete release of the microdisks is expected because the $\text{Ge}_{1-x}\text{Sn}_x$ stack includes three layers with a variable composition. This postetching strain analysis is consistent with systematic studies decoupling Sn content and strain effects on $\text{Ge}_{1-x}\text{Sn}_x$ Raman vibrational modes [18].

To elucidate the effects of composition and strain on the optical properties of the investigated $\text{Ge}_{1-x}\text{Sn}_x$ stacking, an accurate theoretical framework to evaluate the band structure of these multilayers is highly coveted. For instance,

to be able to interpret any optical transition, the band gap in each layer of the TL/ML/BL stacking needs to be estimated as a function of strain and Sn content. To that end, we employ the eight-band $\mathbf{k} \cdot \mathbf{p}$ model framework at 300 K together with the envelope function approximation (EFA) [21]. The eight-band $\mathbf{k} \cdot \mathbf{p}$ $\text{Ge}_{1-x}\text{Sn}_x$ parametrization is based on the work of Chang *et al.* [22], while strain implementation is based on the Bir-Pikus formalism [23]. Additionally, the model solid theory is adopted to estimate the conduction- and valence-band offset profiles of various high-symmetry bands [24,25]. Note that Vegard's law is inaccurate to estimate the band gaps of $\text{Ge}_{1-x}\text{Sn}_x$ compounds due to significant bowing effects of the L and Γ high-symmetry points. To circumvent this limitation, a new set of temperature-dependent bowing parameters at the Γ direction is extracted from our temperature-dependent PL measurement for the strained and relaxed 17 at. % TL as well as the relaxed 13.7 at. % ML. More details about the undertaken fitting procedure are highlighted in Fig. S3 within the Supplemental Material [20]. In a nutshell, at 300 K, the band gap bowing parameters $b_{\Gamma}^{\text{strained-TL}}$ and $b_{\Gamma}^{\text{relaxed-TL}}$ are estimated to be 2.18 and 2.52 eV, respectively, whereas $b_{\Gamma}^{\text{relaxed-ML}}$ is equal to 2.27 eV. The newly extracted Γ - L direction band-gap bowing parameter matches well with values established in the literature [26,27]. The obtained band lineup diagrams for the $\text{Ge}_{0.92}\text{Sn}_{0.08}/\text{Ge}_{0.88}\text{Sn}_{0.12}/\text{Ge}_{0.83}\text{Sn}_{0.17}$ stack are shown in Fig. 2 for the as-grown and relaxed layers at 300 K. From these diagrams, the electron and holes are predicted to diffuse into the utmost 17 at. % layer, as a result of

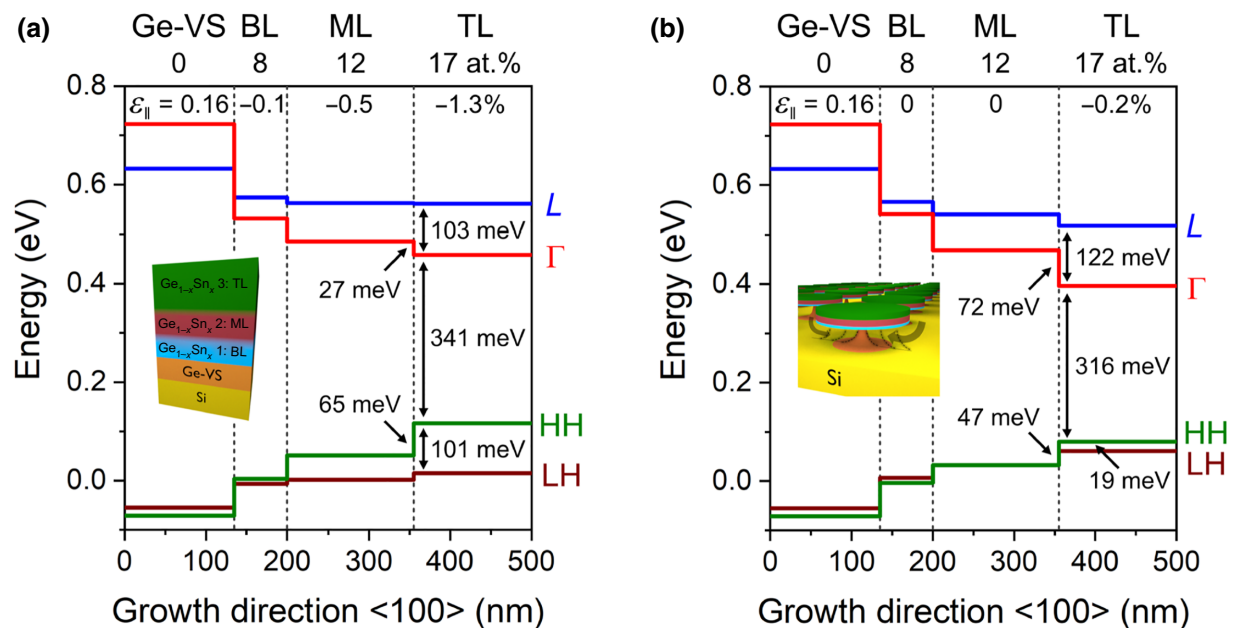


FIG. 2. (a),(b) Calculated $8 \times 8 \mathbf{k} \cdot \mathbf{p}$ band lineup at 300 K for the $\text{Ge}_{0.83}\text{Sn}_{0.17}$ with an in-plane biaxial strain $\varepsilon_{||} = -1.3\%$ (as grown) (a) and $\varepsilon_{||} = -0.2\%$ (microdisks) (b).

the band offset with the 12 at. % ML being equal to 27 and 65 meV for both electrons and heavy holes (HH), respectively. Besides, the strain relaxation (from -1.3% to -0.2%) in the TL layer induces an increase in the energy difference between L and Γ minima in the conduction band $E_g^{L-\Gamma}$ ($= E_g^L - E_g^\Gamma$) of 19 meV, which should enhance band-to-band recombination. Furthermore, the light hole (LH)-heavy hole (HH) splitting is reduced by 82 meV in the TL layer. The valence- (conduction-) band offset between the ML and TL is reduced (increased) by 18 meV (45 meV) due to strain relaxation. Note that Low *et al.* [28] have shown using empirical pseudopotential methods that the band gaps for the unstrained $\text{Ge}_{0.83}\text{Sn}_{0.17}$ at Γ direction to be equal to 0.42 eV (at 4 K). This compares well with our $\mathbf{k} \cdot \mathbf{p}$ parametrization, which gives 0.39 eV. Additionally, based on Gupta *et al.* [8], the as-grown ML layer (12 at. % Sn, -0.54% compressive strain) is expected to have a direct band gap of 0.51 eV (at 0 K), which is in perfect agreement with our $\mathbf{k} \cdot \mathbf{p}$ model, indicating that the ML direct gap transition equals 0.50 eV (at 0 K). Our calculations predict a type-I band alignment in the $\text{Ge}_{1-x}\text{Sn}_x$ multilayer heterostructure, where the radiative recombination should occur in the 17 at. % TL. These calculated results are discussed further below in the light of the optical measurements.

B. Room-temperature PL and transmission measurements for $\text{Ge}_{0.83}\text{Sn}_{0.17}$

To experimentally investigate the effect of strain relaxation on the optical properties of $\text{Ge}_{1-x}\text{Sn}_x$, room-temperature PL and transmission measurements are performed on both as-grown layers and etched microdisk arrays. We first focus on the PL spectra displayed in Fig. 3. In the as-grown $\text{Ge}_{0.83}\text{Sn}_{0.17}$, a main emission peak centered at 0.365 ± 0.005 eV (i.e., $3.4 \mu\text{m}$ wavelength) is recorded with a FWHM of 40–50 meV. A low-intensity emission peak at approximately 0.43 eV is also visible, which could be related either to the optical recombination in the underlying 12 at. % ML or to optical transitions involving the LH band instead of the HH band, as discussed later in the context of data displayed in Fig. 4. Note that the optical emission in this sample mainly originates from the 17 at. % TL [4]. In the microdisks, the optical emission is redshifted to 0.315 ± 0.005 eV (FWHM ~ 60 – 70 meV) compared to the as-grown sample, thus covering a broader range in the MIR up to 4.0 – $4.5 \mu\text{m}$ [Fig. 3(b)]. The measured approximately 50-meV shift (i.e., approximately $0.5 \mu\text{m}$ in wavelength) in the optical emission is induced by the strain relaxation from the as-grown value of -1.3% to -0.2% in the microdisks. The observed increase in the FWHM of the emission peak in the microdisks could be related to small fluctuations in strain between different microdisks, or due to strain-induced HH-LH band splitting

decreasing from approximately 100 meV to approximately 20 meV in the microdisks, which would make the LH also contribute with a new emission peak, partially overlapping with the HH peak and thus broadening the PL spectrum. A comparison with published data must take into consideration both composition and strain values to reach an accurate assessment. Von Driesch *et al.* showed PL emission down to 0.39 eV in partially relaxed $\text{Ge}_{0.86}\text{Sn}_{0.14}$ ($\epsilon_{\parallel} = -0.6\%$) [14], and Calvo *et al.* demonstrated PL emission at approximately 0.37 eV in $\text{Ge}_{0.84}\text{Sn}_{0.16}$ ($\epsilon_{\parallel} \sim -0.8\%$) [3]. These results are consistent with the lower-emission energies observed for our strained and relaxed $\text{Ge}_{0.83}\text{Sn}_{0.17}$ layers, as displayed in Fig. 3. However, the reported optical emission at 0.385 eV in significantly relaxed $\text{Ge}_{0.825}\text{Sn}_{0.175}$ ($\epsilon_{\parallel} \sim -0.3\%$) [2] deviates from this trend and seems to be higher than what it should be. In fact, at nearly the same composition and strain in $\text{Ge}_{0.83}\text{Sn}_{0.17}$ microdisks the emission energy is 0.31 eV (Fig. 3).

The optical emission from $\text{Ge}_{0.83}\text{Sn}_{0.17}$ is then correlated with the absorption measurements performed at 300 K, as shown in Figs. S4–S6 within the Supplemental Material [20]. To provide a precise evaluation of the transmission data and to be able to determine the band gaps of individual layers we define the Napierian absorbance as

$$A_e = \sum_i \alpha_i \times d_i / \cos(\theta_i), \quad (1)$$

where α_i and d_i are the absorption coefficient and thickness of layer i in the stack, respectively, and θ_i the angle with respect to the normal under which the light travels through the layer in the transmission experiment. Surface reflections and interference effects are minimized (see Fig. S6 within the Supplemental Material [20]) by performing transmission experiments at the Brewster angle in an integrating sphere for the as-grown sample as elaborated in Figs. S4–S6 within the Supplemental Material [20]. The microdisks show not to be affected by interference fringes, probably because of misorientation of the individual disks and a slight surface roughness due to etching, therefore they could be measured at normal incidence. The obtained A_e^2 curves are plotted in Fig. 3 together with their respective PL spectra. The A_e^2 spectrum for the as-grown sample clearly shows two onsets that are associated with the TL and ML in the sample where the disks show a single onset associated with the relaxed TL. In a direct band-gap semiconductor, the absorption coefficient α scales as the square root of the energy and linearly with A_e . Therefore, A_e^2 shows a linear behavior with energy, where the band gap is given by the energy-axis crossing. The band gaps determined using this method are also indicated in Fig. 3 as dashed vertical lines. A band gap for the as-grown 17 at. % ($\epsilon_{\parallel} = -1.3\%$) sample of 0.35 ± 0.01 eV is

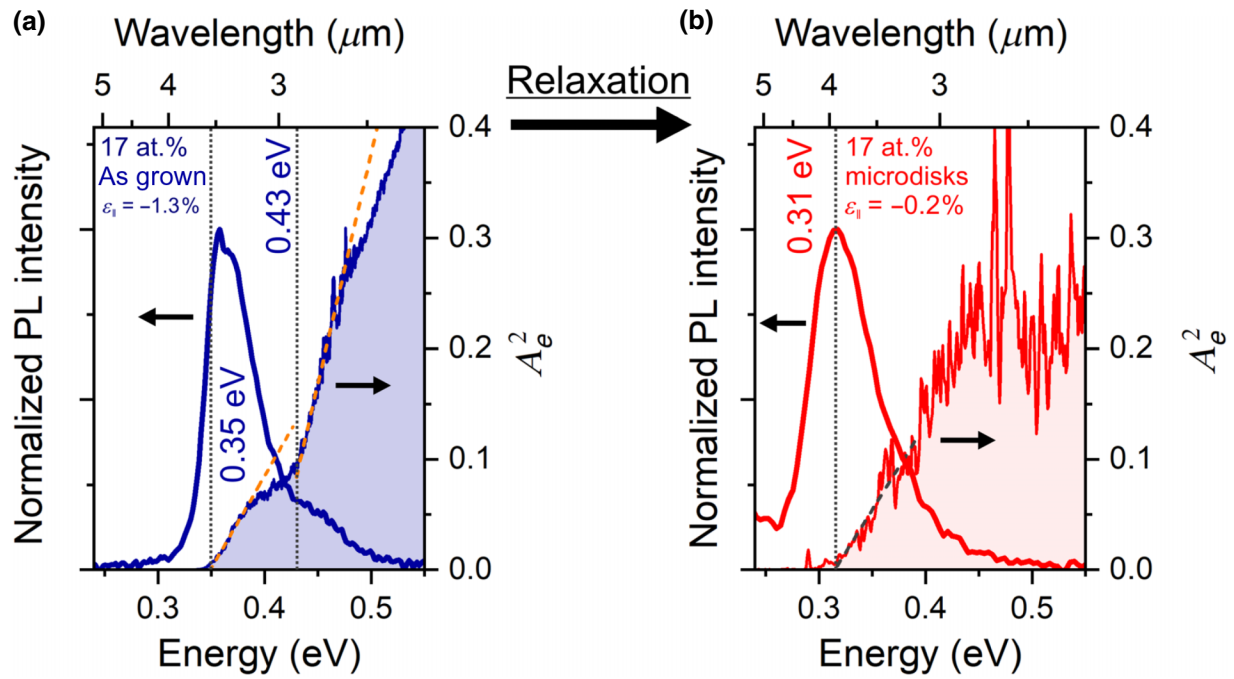


FIG. 3. (a),(b) PL spectra and the Napierian absorbance squared (A_e^2) at 300 K for the $\text{Ge}_{0.83}\text{Sn}_{0.17}$ as-grown (a) and microdisk (b) samples. In the A_e^2 curves, the band gap of the top layer is estimated as the interception of the dashed linear fit with the x axis. For the estimation of the second band gap at 0.43 eV in (a) the contribution of the band gap of the first layers is subtracted.

found, which lies on the rising edge of the corresponding PL signal centered at 0.365 eV as expected. Only a limited contribution from an Urbach tail is visible in the A_e^2 spectrum, in agreement with a previous report on $\text{Ge}_{1-x}\text{Sn}_x$ with a composition up to 10 at. % Sn [29]. Considering the temperature dependence of PL emission (i.e., direct band gap), as discussed later in Figs. 4 and 5, a band gap of approximately 0.29 eV is predicted using the eight-band $\mathbf{k} \cdot \mathbf{p}$ method at 300 K (see Fig. S3 within the Supplemental Material [20]). A small difference between the PL and $\mathbf{k} \cdot \mathbf{p}$ values could arise from the use of a nonoptimized deformation potential constant, due to the scarcity of accurate experimental studies available in the literature. In this work, the deformation potential constants are based on the work of Chang *et al.* [22]. Similarly, the band gap of the 12 at. % Sn ($\epsilon_{||} = -0.5\%$) ML is found to be 0.43 ± 0.01 eV. The extrapolated eight-band $\mathbf{k} \cdot \mathbf{p}$ band-gap value at 300 K is in the 0.34–0.36 eV range, depending on the strain value considered (see Fig. S3 within the Supplemental Material [20]). The 0.43-eV edge is in close agreement with the approximately 0.45 eV estimated for $\text{Ge}_{0.875}\text{Sn}_{0.125}$ ($\epsilon_{||} = -0.3\%$) using reflection measurements by Driesch *et al.* [14]. Nonetheless, the values for both samples agree closely and show the robustness of the method.

In the $\text{Ge}_{0.83}\text{Sn}_{0.17}$ microdisks only a single absorption onset is visible at 0.31 ± 0.01 eV and a rather flat A_e^2 curve is observed above 0.45 eV, without any additional absorption edges at higher energy associated with the 12–8 at. %

Sn layers. The absence of additional absorption onsets can plausibly be attributed to the significantly lower signal-to-noise ratio in the transmission measurements obtained for microdisks because of a reduced absorption volume and the limited intensity of required IR light source. We note that the absorbance of the microdisks shown in Fig. 3(b) (in which the filling factor is taken into account) is similar to the as-grown 17/12 at. % layers (TL/ML) stacking, thus indicating no deterioration of the material quality after the etching process.

C. Temperature-dependent PL measurements in $\text{Ge}_{0.83}\text{Sn}_{0.17}$

To investigate the evolution of the direct band gap with temperature and strain and to identify any possible optically active defect levels, temperature-dependent PL spectra are acquired in the 4–300 K temperature range for both the as-grown and the microdisk sample. These results are displayed in Figs. 4(a)–4(d). For the as-grown $\text{Ge}_{0.83}\text{Sn}_{0.17}$ layer at 4 K [Fig. 4(a)], a single emission peak at 0.413 ± 0.001 eV is observed (FWHM = 19.0 ± 0.5 meV). The symmetric shape of the peak is attributed to limited band filling, indicating a low-carrier injection regime, as shown in the power-dependent PL measurements at 4 K in Fig. S7 within the Supplemental Material [20]. The 4-K PL emission at very low excitation power most likely originates from shallow localized states, such as bound excitons or free-to-bound

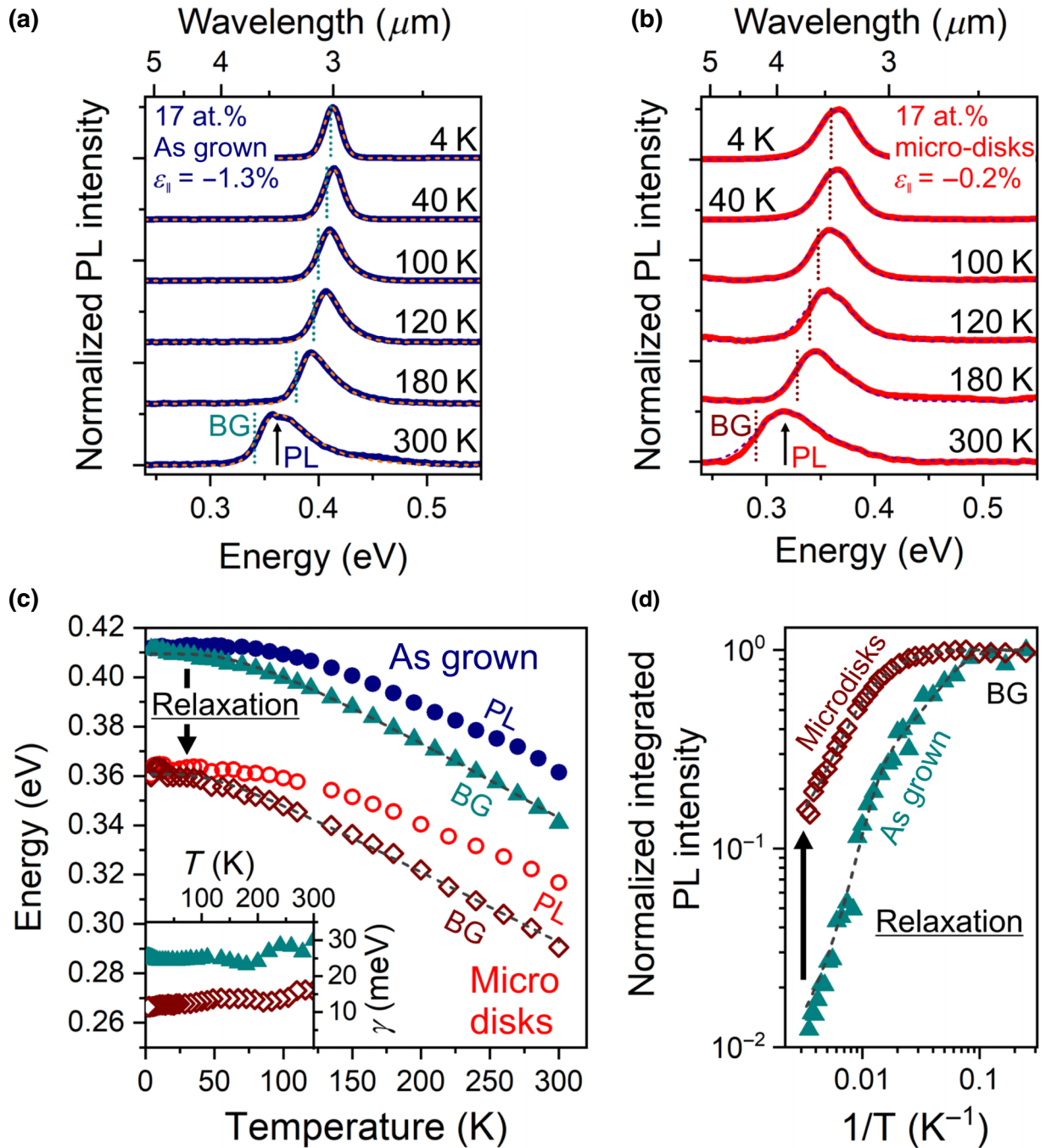


FIG. 4. (a),(b) Temperature-dependent PL measurements in the 4–300 K range for the $\text{Ge}_{0.83}\text{Sn}_{0.17}$ as-grown (a) and the microdisk (b) samples. Spectra are normalized to their own maximum. The line-shape fits using Eq. (2) for each temperature are overlaid as dashed lines, with the band gap as a vertically dotted line. (c) PL emission energy and direct-band-gap (BG) energy as a function of the temperature. Inset: broadening parameter γ [Eq. (2)] as a function of the temperature. (d) Integrated PL intensity, normalized to their respective intensity at 4 K, as a function of the inverse of the temperature extracted from the data shown in (a),(b). The fit of the BG curves in (c) is performed using Eq. (3), while the data in (d) are fitted using Eq. (4) (dashed curves).

transitions, as suggested by the constant emission energy with varying excitation power [30–32]. Local fluctuations in Sn content across the sample and the presence of (low-concentration) impurities are most likely responsible for the observed behavior at low temperatures. At higher excitation power band-to-band emission dominates with

a Burstein-Moss shift of 2–6 meV/decade [33]. Note that no power-dependent energy shift, using similar excitation power densities, is measured at 300 K [4], which further confirms that the direct band gap is maintained at room temperature. In addition, the increase in PL intensity remains linear (slope of approximately 1) even at the

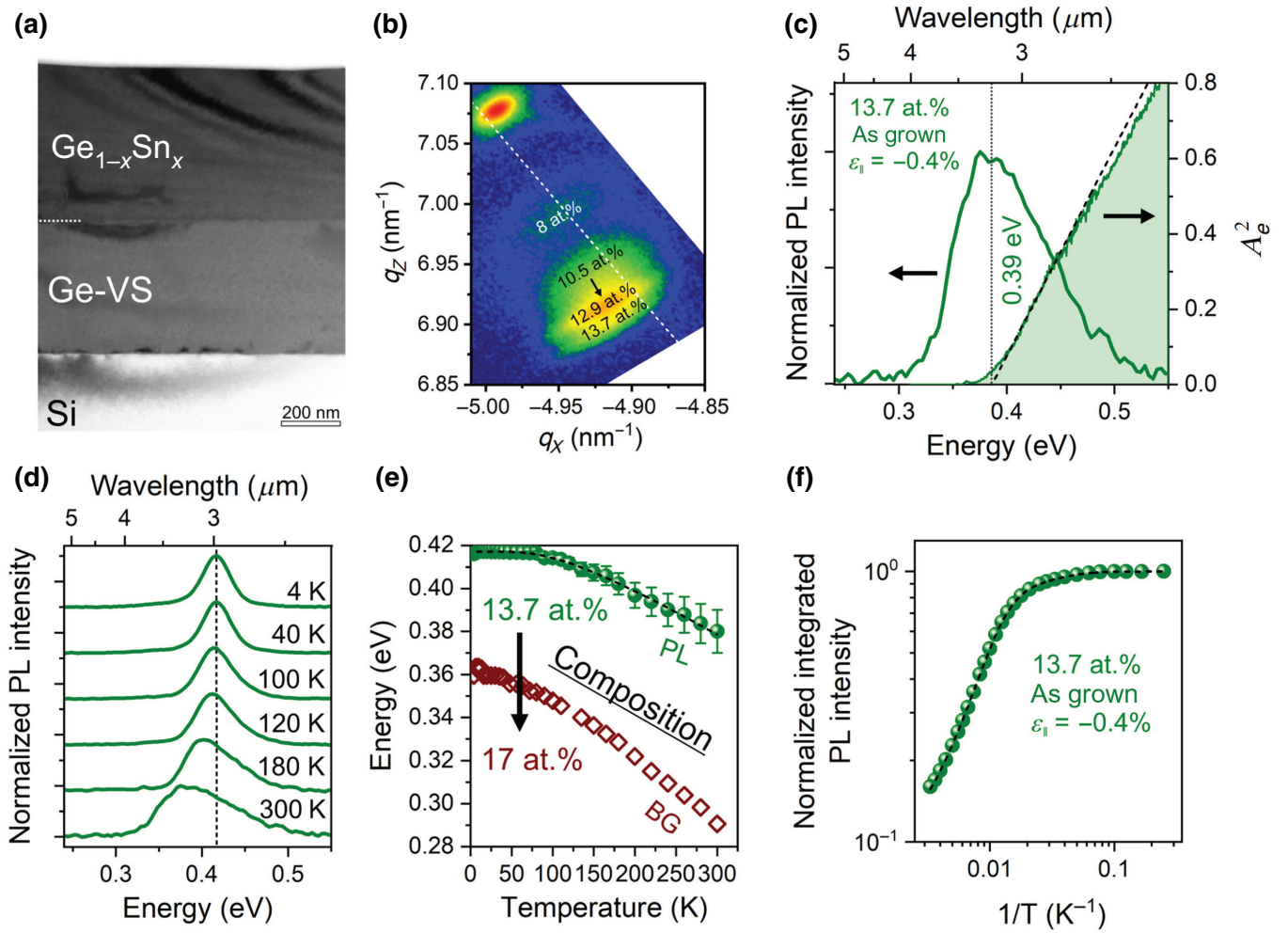


FIG. 5. (a) Cross-section TEM image along the [110] zone axis of the $\text{Ge}_{0.863}\text{Sn}_{0.137}$ sample grown on the Ge-VS/Si substrate. Adapted from Ref. [19]. (b) XRD RSM around the asymmetrical (224) reflection. Adapted from Ref. [19]. (c) PL spectra and Napierian absorbance squared (A_e^2) at 300 K, (d) Temperature-dependent PL measurements in the 4–300 K range. (e)–(f) Emission energy as a function of the temperature (e) and integrated PL intensity as a function of the inverse of the temperature (f) extracted from (d).

highest excitation power densities, indicating that Auger nonradiative recombination does not play a role (see Fig. S7 within the Supplemental Material [20]), which is rather surprising for a narrow-band-gap semiconductor. When the temperature is increased to approximately 50 K, a small blueshift (1.0–1.5 meV) is observed, followed by a progressive redshift as the temperature increases to 300 K, as displayed in Fig. 4(c). No additional peaks are detected in the whole temperature range. The temperature-dependent PL spectra for the $\text{Ge}_{0.83}\text{Sn}_{0.17}$ microdisk arrays are shown in Fig. 4(b). A main emission peak centered at 0.365 ± 0.001 eV (FWHM = 42 ± 3 meV) is detected at 4 K. The emission energy remains constant up to 50 K, followed by a progressive redshift at higher temperatures, reaching 0.315 eV at 300 K. We note that the small blueshift (<2 meV) below 50 K might simply result from the higher FWHM in microdisks compared to as-grown layers. We highlight that the approximately 50 meV energy

difference recorded at 50 K between the as-grown layer and the microdisks is close to the 45 meV observed at 300 K. Thus, the strain in the multilayer structure changes only by a negligible amount with temperature without affecting the band-gap directness across the probed temperature range. The absence of additional PL peaks indicates that the optical recombination dominates in the $\text{Ge}_{0.83}\text{Sn}_{0.17}$ layer regardless of temperature.

To estimate the temperature-dependent band gap from the PL measurements a line-shape model is fitted to the spectra shown in Figs. 4(a) and 4(b) according to the equation:

$$I_{\text{PL}} = A \left[\sqrt{E - E_g} \times \exp\left(-\frac{E}{k_B T}\right) \right] \times \left[\frac{1}{\gamma \sqrt{2\pi}} \exp\left(-\frac{E^2}{2\gamma^2}\right) \right], \quad (2)$$

TABLE I. List of the parameters (a , b , θ_D) extracted from Vina's fit [Eq. (3)] of Figs. 4(c) and 5(e).

	a (eV)	b (eV)	θ_D (K)
As-grown 17.0 at. %	0.443 ± 0.002	0.034 ± 0.002	209 ± 10
Microdisks 17.0 at. %	0.382 ± 0.002	0.021 ± 0.002	146 ± 14
As-grown 13.7 at. %	0.455 ± 0.004	0.040 ± 0.004	436 ± 24

where A is a scaling constant, T is the temperature, and γ is a broadening factor. The first term of the model is given by the joint density of states (JDOS) multiplied by a Boltzmann distribution, assuming low-excitation conditions and parabolic bands. In the second term, broadening mechanisms, such as alloy broadening and strain fluctuations, are taken into account by the convolution of the initial line shape with a Gaussian distribution [34,35]. We note that the best results for the fitting procedure are obtained by setting the carrier and lattice temperatures to be identical, as discussed in more detail in Fig. S8 within the Supplemental Material [20]. The temperature dependence of the PL peak and direct-band-gap energies of $\text{Ge}_{0.83}\text{Sn}_{0.17}$ are displayed in Fig. 4(c). In both as-grown and relaxed samples, the direct band gap is 10–20 meV lower in energy compared to the PL peak across the 4–300 K temperature range. At room temperature, the band gaps of the as-grown sample (0.34 eV) and the microdisk sample (0.29 eV) are only slightly below the values determined using absorption measurements (0.35 ± 0.01 eV and 0.31 ± 0.01 eV, respectively) shown in Fig. 3. This very small shift is probably a result of alloying effects, where PL is more likely to probe the lowest band-gap material and the absorption measurement averages all contributions. Temperature-independent broadening factors γ are obtained for both the as-grown ($\gamma = 13 \pm 1$ meV) and the microdisk sample ($\gamma = 25 \pm 2$ meV), as plotted in the inset of Fig. 4(c). The increased broadening in the microdisks with respect to the as-grown sample can be attributed to small strain fluctuations that are introduced in the etching process. Next, the fit of the band gap as a function of temperature is performed using Vina's equation [36]:

$$E_g = a - b \left[1 + \frac{2}{\exp(\theta_D/T) - 1} \right], \quad (3)$$

where a is a constant, b is the strength of the electron-phonon interaction, and θ_D is the mean temperature of the phonons contributing to the scattering process. The values obtained using Eq. (3) are listed in Table I. When compared to the widely used Varshi's equation [37], Vina's equation provides higher fit accuracy in the high-temperature regime for materials with lower θ_D like Ge (374 K) and α -Sn (270 K) as compared to Si (640 K) [36,38].

The integrated PL intensities, as a function of the inverse of temperature, for the direct band gap of the as-grown

$\text{Ge}_{0.83}\text{Sn}_{0.17}$ layer and the microdisk array are displayed in Fig. 4(d). The data are normalized to the intensity measured at 4 K for each set of samples. Overall, the PL emission exhibits the same qualitative behavior for both samples, viz., a monotonous decrease as temperature increases, which becomes more pronounced above 100 K. At 300 K, a decrease in the PL intensity to 1%–2% compared to the 4-K intensity is measured for the as-grown layer, whereas in the microdisk array this decrease is rather limited to 10%–20% suggesting an increase in the quantum efficiency in strain-relaxed microdisks. Since no sudden changes in both PL emission energy and intensity are observed across the 4–300 K range, direct-band-gap radiative recombination is the dominating mechanism in the as-grown and microdisk samples [39,40], with a negligible amount of impurity ionization [41].

To shed more light on the nonradiative processes in these samples, the integrated PL intensities are fitted with Arrhenius functions [dashed lines in Fig. 4(d)] considering two active nonradiative recombination channels, according to

$$I = 1 / \left[1 + c_1 \times \exp\left(-\frac{E_a^1}{kT}\right) + c_2 \times \exp\left(-\frac{E_a^2}{kT}\right) \right], \quad (4)$$

where c_1 and c_2 are constants, E_a^1 and E_a^2 are the activation energies, and k is the Boltzmann constant [42]. This set of parameters contains rich information on physical recombination processes [40]. The results obtained from the fit using Eq. (4) are listed in Table II. The first activation energy E_a^1 is approximately 5 meV in as-grown layers and microdisks suggesting a common loss mechanism for the two materials. This loss could be facilitated by a shallow impurity level ionizing at low temperatures, perhaps related to the observed 1–2 meV blueshift in as-grown layer at low temperatures. Thus, in $\text{Ge}_{0.83}\text{Sn}_{0.17}$ the recorded PL below 50 K is most likely due to a 1–4 meV shallow level, whereas band-to-band recombination is observed at higher temperatures [32,41]. The second activation energy E_a^2 indicates the presence of a 20–40 meV higher-energy nonradiative recombination channel, which could originate from intervalley tunneling of electrons into the L minimum or from a deeper impurity level within the band gap. The calculated band diagram of $\text{Ge}_{0.83}\text{Sn}_{0.17}$ (Fig. 2) indicates that the L minimum is approximately 103 meV and approximately 122 meV higher compared to the Γ minimum in as-grown (strained) and microdisk (relaxed) samples, respectively. Thus, intervalley tunneling is an unlikely carrier diffusion process in $\text{Ge}_{0.83}\text{Sn}_{0.17}$ across the entire 4–300 K temperature range. Other possible loss mechanisms are surface traps or defects within the layer (i.e., impurities and point defects), which are both thermally activated sources of nonradiative recombination. Herein, it is worthwhile to mention

that no impurities are observed in atom-probe tomography (APT) measurements (detection limit approximately $1 \times 10^{17} \text{ cm}^{-3}$) [43] of $\text{Ge}_{0.83}\text{Sn}_{0.17}$ layer (Fig. S9 within the Supplemental Material [20]) [4]. However, point defects in a semiconductor, such as vacancies and vacancy complexes, can also affect the optical properties due to carrier trapping [44–46]. The presence of divacancies and, to a limited extent, of vacancy clusters at room temperature has been recently confirmed in as-grown GeSn layers [19] and they might contribute to the activation energy E_a^2 as an additional nonradiative recombination channel. Another plausible interpretation for E_a^2 would be the loss of carriers due to diffusion from the 17 at. % TL to the 12 at. % ML, where they (partially) recombine nonradiatively. In the as-grown sample, the calculated conduction-band offset between TL and ML, $\Delta E_c = 27 \text{ meV}$, (Fig. 2) is close to the activation energy E_a^2 ($32 \pm 7 \text{ meV}$) as provided by the fit. This means that electrons can diffuse to the ML, where an overall quench in PL will already be observed when only one of the two charge carriers leaks away. With this mechanism in mind, one might argue that the observed approximately 0.45 eV PL peak in the as-grown $\text{Ge}_{0.83}\text{Sn}_{0.17}$ above the 180 K [Fig. 4(a)] sample could be associated with emission from the 12 at. % ML instead of a contribution of LH-HH splitting in the strained 17 at. % TL. In the relaxed ML layer, the conduction- and valence-band offsets (at 0 K), respectively, equal to $\Delta E_c = 78 \text{ meV}$ and $\Delta E_v = 30 \text{ meV}$, changes such that only holes can be thermally excited into the ML.

D. Effect of composition on the optical properties

In addition to the postgrowth relaxation described above and for the sake of comparison, we examine in the following strain relaxation achieved during epitaxial growth using a compositionally graded $\text{Ge}_{1-x}\text{Sn}_x$ layer. In this configuration, the lattice parameter gradually increases throughout the layer thickness and additional Sn atoms are incorporated in the growing layer, which results in a graded profile [7]. To put the effect of strain relaxation and composition in perspective, we compare the results in Figs. 3 and 4 with a lower Sn-content graded $\text{Ge}_{0.863}\text{Sn}_{0.137}$ sample that is relatively highly relaxed ($\varepsilon_{\parallel} = -0.4 \%$) and shows PL emission at a similar energy to that of as-grown $\text{Ge}_{0.83}\text{Sn}_{0.17}$ sample. The high relaxation on the other hand makes a direct comparison with the previously discussed microdisks possible while considering the difference in composition. The compositionally graded growth starts with an approximately 60-nm-thick nucleation layer with 8 at. % Sn, followed by an approximately 700 nm-thick $\text{Ge}_{1-x}\text{Sn}_x$ layer [Fig. 5(a)]. In this layer, a graded composition (60–400 nm) from 10.5 to 12.9 at. % is observed, followed by a uniform composition (400–700 nm) of 13.7 at. %. The graded and uniform layers are also visible in

the RSM map in Fig. 5(b), as described in Refs. [7,19]. The residual in-plane strain across the $\text{Ge}_{1-x}\text{Sn}_x$ layers is lower than -0.4% , thus indicating a high degree of strain relaxation. Room-temperature PL spectra measured for this sample are plotted in Fig. 5(c). A main emission peak centered at $0.380 \pm 0.010 \text{ eV}$ is observed, however, with a relatively large FWHM of approximately 100 meV that most likely results from the gradual change in the band-gap energy across the graded layer (i.e., emission from the lower Sn content layers). Note that in the as-grown $\text{Ge}_{0.83}\text{Sn}_{0.17}$ sample with a uniform composition, the FWHM is half of the value obtained in the compositionally graded $\text{Ge}_{0.863}\text{Sn}_{0.137}$. Additionally, the 0.38-eV emission in $\text{Ge}_{0.863}\text{Sn}_{0.137}$ is in line with the emission at approximately 0.39 eV reported for partially relaxed $\text{Ge}_{0.86}\text{Sn}_{0.14}$ ($\varepsilon_{\parallel} = -0.6 \%$) [14] and in lower Sn content $\text{Ge}_{0.893}\text{Sn}_{0.107}$ microdisks with a 0.45% tensile strain induced by external SiN stressors [15].

In the transmission data and corresponding Napierian absorbance squared curve [Fig. 5(c)], the direct-band-gap absorption edge for the layer with a composition of 13.7 at. % is visible at $0.39 \pm 0.01 \text{ eV}$, while no other onsets are visible due to the graded Sn composition. The very good agreement between the PL and absorption data demonstrates that the band-to-band radiative recombination takes place in the upmost $\text{Ge}_{0.863}\text{Sn}_{0.137}$ layer. It is worthwhile to note that no reliable line-shape fitting procedure could be performed because of the graded composition in this sample resulting in a gradual change in the band-gap energy. Therefore, the PL peak position is used in the following data analysis. In temperature-dependent PL measurements [Figs. 5(d)–5(f)], a single emission peak is observed throughout the 4–300 K range. At 4 K, the emission peak is centered at $0.416 \pm 0.001 \text{ eV}$ (FWHM = $42.0 \pm 0.5 \text{ meV}$) and its width is $2 \times$ larger than that of the $\text{Ge}_{0.83}\text{Sn}_{0.17}$ layer. This difference in FWHM remains similar to that observed at room temperature. When the temperature is increased, the emission energy in $\text{Ge}_{0.863}\text{Sn}_{0.137}$ remains unaffected up to 80 K, followed by a progressive decrease at higher temperature, reaching 0.381 eV at 300 K. When the temperature rises from 4 to 300 K, the integrated PL intensity drops to approximately 15% of its initial value, which is very similar to what is observed in relaxed $\text{Ge}_{0.83}\text{Sn}_{0.17}$ microdisks [Fig. 4(d)]. The values estimated from Vina's fit [Eq. (3), Table I] and activation energies E_a^1 and E_a^2 values from the Arrhenius plot [Eq. (4), Table II] are in the same range as those obtained for $\text{Ge}_{0.83}\text{Sn}_{0.17}$. Therefore, the graded composition in the as-grown $\text{Ge}_{0.863}\text{Sn}_{0.137}$ has a negligible effect on the energy of shallow levels, while it increases the emission linewidth by a factor 2 at all temperatures when compared to $\text{Ge}_{0.83}\text{Sn}_{0.17}$. Despite the broader PL peak, the strain relaxation resulting from the graded composition might promote optical recombination and minimize nonradiative recombination channels, in analogy to the $\text{Ge}_{0.83}\text{Sn}_{0.17}$ microdisk arrays discussed

TABLE II. List of the parameters (E_a^1 , E_a^2 , c_1 , c_2) extracted from the fit considering two nonradiative recombination channels [Eq. (4)] of Figs. 4(d) and 5(f).

	E_a^1 (meV)	c_1	E_a^2 (meV)	c_2
As-grown 17 at. %	3.8 ± 0.5	4.2 ± 0.8	32 ± 7	199 ± 160
Microdisks 17 at. %	9 ± 1	1.4 ± 0.3	34 ± 3	15 ± 2
As-grown 13.7 at. %	4.7 ± 0.2	0.42 ± 0.02	25.6 ± 0.2	13.5 ± 0.1

above where a similar PL quenching to approximately 10% of its initial value is observed from 4 to 300 K [Fig. 4(d)]. Thus, the optical properties of $\text{Ge}_{1-x}\text{Sn}_x$ are enhanced by strain relaxation, regardless of the method used to reduce strain in the epilayer.

Curiously enough, the negligible role of defect- and impurity-related emission seen in the data exhibited in Figs. 4 and 5 remains one of the striking observations when the current work is compared to the literature despite the higher Sn content in the investigated layers. In fact, the few available studies highlighted clear contributions from dislocations and impurities on the temperature-dependent PL emission in $\text{Ge}_{1-x}\text{Sn}_x$ at Sn content close or above 10 at. % [39,41,47]. For instance, Pezzoli *et al.* discussed the trapping of carriers in dislocations observed at low temperature in indirect band gap $\text{Ge}_{0.91}\text{Sn}_{0.09}$, indicating that subsequent thermal detrapping seems to result in an enhanced PL intensity due to increased radiative band-to-band recombination [39]. Defect-related deep levels (approximately 150 meV) are also observed in pseudomorphic (<50-nm-thick) $\text{Ge}_{0.875}\text{Sn}_{0.125}$ layers, which are possibly associated to the presence of dislocations in $\text{Ge}_{1-x}\text{Sn}_x/\text{Ge-VS}$ heterostructure [47]. For thicker layers (>500 nm thick), the emission from deep levels is absent, however, an approximately 8-meV blueshift of the PL emission energy is clearly observed when temperature increases from 4 to 100 K ($E_a \sim 32$ meV), followed by a rapid quenching of the emission at higher temperatures. This behavior indicates the presence of shallow impurity levels within the band gap that are ionized above 100 K (shallow level). Impurity ionization (20–30 meV) into the band-gap emission with increasing temperature is also observed in $\text{Ge}/\text{Ge}_{0.87}\text{Sn}_{0.13}$ core-shell nanowires [41] and in $\text{Ge}_{0.81}\text{Sn}_{0.19}$ nanowires [48]. Obviously, any explanation of these differences is challenging at this stage, and residual impurities are most likely present in our samples with concentrations lower than the detection limit (approximately $1 \times 10^{17} \text{ cm}^{-3}$) of APT (Fig. S9 within the Supplemental Material [20]). However, it is sensible to consider the influence of growth conditions on the possible incorporation of point defects and impurities. In this regard, one can invoke the growth rate as an obvious difference as the layers investigated in this work are grown at a rate of approximately 1.5 nm/min, which is approximately 10 times lower than comparable samples from other research groups [7]. Nonetheless, the

growth of $\text{Ge}_{1-x}\text{Sn}_x$ shells around Ge nanowires is performed at a lower growth rate (<1 nm/min) [41] for which PL emission associated with deep levels is observed, thus hinting to other possible critical factors. As a matter of fact, further in-depth investigations are needed to decipher the key parameters affecting the impurity and vacancy incorporation, their complexes, and their role in shaping the optical properties of $\text{Ge}_{1-x}\text{Sn}_x$ semiconductors.

IV. CONCLUSIONS

In this work, we demonstrate that room-temperature optical emission in $\text{Ge}_{1-x}\text{Sn}_x$ can be extended to longer wavelengths in the midinfrared range by independently controlling strain and composition. The observed single-peak PL emission at 300 K in the as-grown $\text{Ge}_{0.83}\text{Sn}_{0.17}$ shifts from 0.365 to 0.315 eV (i.e., approximately 3.4 μm to approximately 4.0 μm wavelength) by releasing most of the -1.3% compressive strain in underetched microdisks, in qualitative agreement with $8 \times 8 \text{ k} \cdot \text{p}$ band-structure calculations. No additional PL peaks are visible when cooling down as-grown and microdisk samples to 4 K, suggesting the absence of defect- and impurity-related emission and that direct-band-gap emission is preserved. By increasing the temperature from 4 to 300 K, the PL intensity is reduced to 1%–2% and 10%–20% of its initial value in as-grown and relaxed $\text{Ge}_{0.83}\text{Sn}_{0.17}$, respectively. Therefore, carrier losses into thermally activated nonradiative recombination channels are minimized by promoting strain relaxation. These observations are confirmed in $\text{Ge}_{0.863}\text{Sn}_{0.137}$, where a significant strain relaxation is obtained as a result of a graded composition. However, a broader 300-K PL emission peak at 0.380 eV is obtained as compared to $\text{Ge}_{0.83}\text{Sn}_{0.17}$ with uniform composition. Regardless of strain and composition, impurities and other nonradiative recombination channels seem to have no detrimental effect on PL emission. Absorption measurements performed at 300 K give a deep insight into the absorption process in $\text{Ge}_{1-x}\text{Sn}_x$ multilayer structures and confirm the effect of strain relaxation in inducing a redshift of the absorption edge. Additionally, these analyses also demonstrate the band-gap directness in strained and relaxed $\text{Ge}_{0.83}\text{Sn}_{0.17}$ layers as well as in the compositionally graded $\text{Ge}_{0.863}\text{Sn}_{0.137}$. Thus, the control of both strain and composition uniformity is highly useful for engineering the emission operational range and linewidth in

Ge_{1-x}Sn_x optoelectronic devices [17]. Applications requiring a narrower spectral range would benefit from the use of uniform, Ge_{1-x}Sn_x layers, where a large amount of Sn can be incorporated while avoiding phase segregation [49]. Whereas, a graded composition would enhance absorption at a larger layer thickness and cover a broader spectral range.

ACKNOWLEDGMENTS

The authors thank J. Bouchard for the technical support with the CVD system. O.M. acknowledges support from NSERC Canada (Discovery, SPG, and CRD Grants), Canada Research Chairs, Canada Foundation for Innovation, Mitacs, PRIMA Québec, and Defence Canada (Innovation for Defence Excellence and Security, IDEaS). S.A. acknowledges support from Fonds de recherche du Québec-Nature et technologies (FRQNT, PBEEE scholarship). A.D. acknowledges support from the NWO gravity program.

NOTES

The authors declare no competing financial interest.

- [1] S. Wirths, R. Geiger, N. von den Driesch, G. Mussler, T. Stoica, S. Mantl, Z. Ikonic, M. Luysberg, S. Chiussi, J. M. Hartmann, H. Sigg, J. Faist, D. Buca, and D. Grützmacher, Lasing in direct-bandgap GeSn alloy grown on Si, *Nat. Photonics* **9**, 88 (2015).
- [2] J. Margetis, S. Al-Kabi, W. Du, W. Dou, Y. Zhou, T. Pham, P. Grant, S. Ghetmiri, A. Mosleh, B. Li, J. Liu, G. Sun, R. Soref, J. Tolle, M. Mortazavi, and S.-Q. Yu, Si-Based GeSn lasers with wavelength coverage of 2–3 μm and operating temperatures up to 180K, *ACS Photonics* **5**, 827 (2018).
- [3] V. Reboud, A. Gassenq, N. Pauc, J. Aubin, L. Milord, Q. M. Thai, M. Bertrand, K. Guillois, D. Rouchon, J. Rothman, T. Zabel, F. Armand Pilon, H. Sigg, A. Chelnokov, J. M. Hartmann, and V. Calvo, Optically pumped GeSn microdisks with 16% Sn lasing at 3.1 μm up to 180 K, *Appl. Phys. Lett.* **111**, 092101 (2017).
- [4] S. Assali, J. Nicolas, S. Mukherjee, A. Dijkstra, and O. Moutanabbir, Atomically uniform Sn-rich GeSn semiconductors with 3.0–3.5 μm room-temperature optical emission, *Appl. Phys. Lett.* **112**, 251903 (2018).
- [5] A. Attiaoui, S. Wirth, A.-P. Blanchard-Dionne, M. Meunier, J. M. Hartmann, D. Buca, and O. Moutanabbir, Extreme IR absorption in group IV-SiGeSn core-shell nanowires, *J. Appl. Phys.* **123**, 223102 (2018).
- [6] J. Margetis, S.-Q. Q. Yu, N. Bhargava, B. Li, W. Du, and J. Tolle, Strain engineering in epitaxial Ge_{1-x}Sn_x: A path towards low-defect and high Sn-content layers, *Semicond. Sci. Technol.* **32**, 124006 (2017).
- [7] S. Assali, J. Nicolas, and O. Moutanabbir, Enhanced Sn incorporation in GeSn epitaxial semiconductors via strain relaxation, *J. Appl. Phys.* **125**, 025304 (2019).
- [8] S. Gupta, B. Magyari-Köpe, Y. Nishi, and K. C. Saraswat, Achieving direct band Gap in germanium through integration of Sn alloying and external strain, *J. Appl. Phys.* **113**, 073707 (2013).
- [9] A. Attiaoui and O. Moutanabbir, Indirect-to-Direct band Gap transition in relaxed and strained Ge_{1-x-y}Si_xSn_y ternary alloys, *J. Appl. Phys.* **116**, 063712 (2014).
- [10] M. P. Polak, P. Scharoch, and R. Kudrawiec, The electronic band structure of Ge_{1-x}Sn_x in the full composition range: Indirect, direct, and inverted gaps regimes, band offsets, and the burstein-moss effect, *J. Phys. D: Appl. Phys.* **50**, 195103 (2017).
- [11] D. Stange, N. von den Driesch, T. Zabel, F. Armand-Pilon, D. Rainko, B. Marzban, P. Zaumseil, J.-M. Hartmann, Z. Ikonic, G. Capellini, S. Mantl, H. Sigg, J. Witzens, D. Grützmacher, and D. Buca, Gesn/SiGeSn heterostructure and multi quantum well lasers, *ACS Photonics* **5**, 4628 (2018).
- [12] J. Chrétien, N. Pauc, F. Armand Pilon, M. Bertrand, Q.-M. Thai, L. Casiez, N. Bernier, H. Dansas, P. Gergaud, E. Delamadeleine, R. Khazaka, H. Sigg, J. Faist, A. Chelnokov, V. Reboud, J.-M. Hartmann, and V. Calvo, Gesn lasers covering a wide wavelength range thanks to uniaxial tensile strain, *ACS Photonics* **6**, 2462 (2019).
- [13] Y. Zhou, Y. Miao, S. Ojo, H. Tran, G. Abernathy, J. M. Grant, S. Amoah, G. Salamo, W. Du, J. Liu, J. Margetis, J. Tolle, Y.-H. Zhang, G. Sun, R. A. Soref, B. Li, and S.-Q. Yu, Electrically injected GeSn lasers on Si operating up to 100K, *Optica* **7**, 924 (2020).
- [14] N. Von Den Driesch, D. Stange, S. Wirths, G. Mussler, B. Hollander, Z. Ikonic, J. M. Hartmann, T. Stoica, S. Mantl, D. Grützmacher, and D. Buca, Direct bandgap group IV epitaxy on Si for laser applications, *Chem. Mater.* **27**, 4693 (2015).
- [15] R. W. Millar, D. C. S. Dumas, K. F. Gallacher, P. Jahan-dar, C. MacGregor, M. Myronov, and D. J. Paul, Mid-Infrared light emission >3 μm wavelength from tensile strained GeSn microdisks, *Opt. Express* **25**, 25374 (2017).
- [16] D. Stange, S. Wirths, R. Geiger, C. Schulte-Braucks, B. Marzban, N. V. Den Driesch, G. Mussler, T. Zabel, T. Stoica, J.-M. Hartmann, S. Mantl, Z. Ikonic, D. Grützmacher, H. Sigg, J. Witzens, and D. Buca, Optically pumped GeSn microdisk lasers on Si, *ACS Photonics* **3**, 1279 (2016).
- [17] M. R. M. Atalla, S. Assali, A. Attiaoui, C. Lemieux-Leduc, A. Kumar, S. Abdi, and O. Moutanabbir, All-group IV membrane room-temperature mid-infrared photodetector, *Adv. Funct. Mater.* **31**, 2006329 (2021).
- [18] É Bouthillier, S. Assali, J. Nicolas, and O. Moutanabbir, Decoupling the effects of composition and strain on the vibrational modes of GeSn semiconductors, *Semicond. Sci. Technol.* **35**, 095006 (2020).
- [19] S. Assali, M. Elsayed, J. Nicolas, M. O. Liedke, A. Wagner, M. Butterling, R. Krause-Rehberg, and O. Moutanabbir, Vacancy complexes in nonequilibrium germanium-Tin semiconductors, *Appl. Phys. Lett.* **114**, 251907 (2019).
- [20] See the Supplemental Material at <http://link.aps.org/supplemental/10.1103/PhysRevApplied.15.024031> for additional information on the structural characterization, optical measurements, and theoretical calculations.

- [21] T. B. Bahder, Erratum: Eight-band Kp model of strained zinc-blende crystals (physical review B (1990) 41, 11, (1992)), *Phys. Rev. B* **46**, 9913 (1992).
- [22] G.-E. Chang, S.-W. Chang, and S. L. Chuang, Strain-Balanced Ge_zSn_{1-z}/SixGe_{1-x}Sn_{1-x-y} multiple-quantum-well lasers, *IEEE J. Quantum Electron.* **46**, 1813 (2010).
- [23] G. L. Bir and G. E. Pikus, *Symmetry and Strain-Induced Effects in Semiconductors. Translated From Russian by P. Shelnitz* (Wiley, New York, 1974).
- [24] C. G. Van de Walle and R. M. Martin, Theoretical calculations of heterojunction discontinuities in the Si/Ge system, *Phys. Rev. B* **34**, 5621 (1986).
- [25] C. G. de Walle, Band lineups and deformation potentials in the model-solid theory, *Phys. Rev. B* **39**, 1871 (1989).
- [26] A. Gassenq, L. Milord, J. Aubin, K. Guilloy, S. Tardif, N. Pauc, J. Rothman, A. Chelnokov, J. M. Hartmann, V. Reboud, and V. Calvo, Gamma bandgap determination in pseudomorphic GeSn layers grown on Ge with up to 15% Sn content, *Appl. Phys. Lett.* **109**, 242107 (2016).
- [27] H. Lin, R. Chen, W. Lu, Y. Huo, T. I. Kamins, and J. S. Harris, Investigation of the direct band gaps in Ge_{1-x}Sn_x alloys with strain control by photoreflectance spectroscopy, *Appl. Phys. Lett.* **100**, 102109 (2012).
- [28] K. Lu Low, Y. Yang, G. Han, W. Fan, and Y.-C. Yeo, Electronic band structure and effective mass parameters of Ge_{1-x}Sn_x alloys, *J. Appl. Phys.* **112**, 103715 (2012).
- [29] H. Tran, W. Du, S. A. Ghetmiri, A. Mosleh, G. Sun, R. A. Soref, J. Margetis, J. Tolle, B. Li, H. A. Naseem, and S.-Q. Yu, Systematic study of Ge_{1-x}Sn_x absorption coefficient and refractive index for the device applications of Si-based optoelectronics, *J. Appl. Phys.* **119**, 103106 (2016).
- [30] T. Schmidt, K. Lischka, and W. Zulehner, Excitation-Power dependence of the near-band-edge photoluminescence of semiconductors, *Phys. Rev. B* **45**, 8989 (1992).
- [31] U. Kaufmann, M. Kunzer, M. Maier, H. Obloh, A. Ramakrishnan, B. Santic, and P. Schlotter, Nature of the 2.8 eV photoluminescence band in Mg doped GaN, *Appl. Phys. Lett.* **72**, 1326 (1998).
- [32] S. Assali, J. Greil, I. Zardo, A. Belabbes, M. W. A. De Moor, S. Koelling, P. M. Koenraad, F. Bechstedt, E. P. A. M. Bakkers, and J. E. M. Haverkort, Optical study of the band structure of wurtzite GaP nanowires, *J. Appl. Phys.* **120**, 044304 (2016).
- [33] E. Burstein, Anomalous optical absorption limit in InSb, *Phys. Rev.* **93**, 632 (1954).
- [34] E. F. Schubert, E. O. Göbel, Y. Horikoshi, K. Ploog, and H. J. Queisser, Alloy broadening in photoluminescence spectra of Al_xGa_{1-x}As, *Phys. Rev. B* **30**, 813 (1984).
- [35] D. Ouadjaout and Y. Marfaing, Localized excitons in II-VI semiconductor alloys: Density-of-states model and photoluminescence line-shape analysis, *Phys. Rev. B* **41**, 12096 (1990).
- [36] L. Viña, S. Logothetidis, and M. Cardona, Temperature dependence of the dielectric function of germanium, *Phys. Rev. B* **30**, 1979 (1984).
- [37] P. Y. Varshni, Temperature dependence of the energy Gap in semiconductors, *Physica* **34**, 149 (1967).
- [38] O. Madelung, U. Rössler, and M. Schulz, *Group IV Elements, IV-IV and III-V Compounds. Part b - Electronic, Transport, Optical and Other Properties*, Vol. b (Springer-Verlag, Berlin/Heidelberg, 2002).
- [39] F. Pezzoli, A. Giorgioni, D. Patchett, and M. Myronov, Temperature-Dependent photoluminescence characteristics of GeSn epitaxial layers, *ACS Photonics* **3**, 2004 (2016).
- [40] M. A. Reshchikov, Temperature dependence of defect-related photoluminescence in III-V and II-VI semiconductors, *J. Appl. Phys.* **115**, 012010 (2014).
- [41] S. Assali, A. Dijkstra, A. Li, S. Koelling, M. A. Verheijen, L. Gagliano, N. von den Driesch, D. Buca, P. M. Koenraad, J. E. M. Haverkort, and E. P. A. M. Bakkers, Growth and optical properties of direct band Gap Ge/Ge_{0.87}Sn_{0.13} core/shell nanowire arrays, *Nano Lett.* **17**, 1538 (2017).
- [42] M. Leroux, N. Grandjean, B. Beaumont, G. Nataf, F. Semond, J. Massies, and P. Gibart, Temperature quenching of photoluminescence intensities in undoped and doped GaN, *J. Appl. Phys.* **86**, 3721 (1999).
- [43] S. Koelling, A. Li, A. Cavalli, S. Assali, D. Car, S. Gazibegovic, E. P. A. M. Bakkers, and P. M. Koenraad, Atom-by-Atom analysis of semiconductor nanowires with parts Per million sensitivity, *Nano Lett.* **17**, 599 (2017).
- [44] W. P. Bai, N. Lu, A. Ritenour, M. L. Lee, D. A. Antoniadis, and D.-L. Kwong, Ge N-MOSFETs on lightly doped substrates with high- κ dielectric and TaN gate, *IEEE Electron Device Lett.* **27**, 175 (2006).
- [45] M. Christian Petersen, A. Nylandsted Larsen, and A. Mesli, Divacancy defects in germanium studied using deep-level transient spectroscopy, *Phys. Rev. B* **82**, 075203 (2010).
- [46] C. G. Van de Walle and J. Neugebauer, First-Principles calculations for defects and impurities: Applications to III-nitrides, *J. Appl. Phys.* **95**, 3851 (2004).
- [47] D. Stange, S. Wirths, N. Von Den Driesch, G. Mussler, T. Stoica, Z. Ikonik, J. M. Hartmann, S. Mantl, D. Grützmacher, and D. Buca, Optical transitions in direct-bandgap Ge_{1-x}Sn_x alloys, *ACS Photonics* **2**, 1539 (2015).
- [48] M. S. Seifner, A. Dijkstra, J. Bernardi, A. Steiger-Thirsfeld, M. Sistani, A. Lugstein, J. E. M. Haverkort, and S. Barth, *Epitaxial Ge_{0.81}Sn_{0.19} Nanowires for Nanoscale Mid-Infrared Emitters*, *ACS Nano* **acs.nano.9b02843** (2019).
- [49] J. Nicolas, S. Assali, S. Mukherjee, A. Lotnyk, and O. Moutanabbir, Dislocation pipe diffusion and solute segregation during the growth of metastable GeSn, *Cryst. Growth Des.* **20**, 3493 (2020).